

Use of DL-EPR Test to Assess Sensitization Resistance of AISI 409M Grade Ferritic Stainless Steel Joints

A.K. Lakshminarayanan and V. Balasubramanian

(Submitted December 17, 2012; in revised form February 28, 2013; published online March 16, 2013)

The susceptibility of 409M grade ferritic stainless steels to sensitization due to welding was investigated. Joints were fabricated by gas tungsten arc welding, friction stir welding, laser beam welding, and electron beam welding processes. Double loop electrochemical potentiokinetic reactivation test was carried out for determining the degree of sensitization of welded joints. The experimental result reveals that, the friction stir welded joint is less prone to sensitization, when compared to the other joints.

Keywords ferritic stainless steel, sensitization, welding

1. Introduction

Ferritic stainless steels (FSSs) are normally used in a mildly corrosive atmosphere for chemical processing equipment, furnace parts, heat exchangers, oil burner parts, petroleum refining equipment, protection tubes, recuperates, storage vessels, electrical appliances, solar water heaters, and household appliances (Ref 1). Due to the increasing use of fusion joining in such industrial applications, the welding metallurgy of FSS has drawn much attention recently.

However, joining of FSS is faced with the problem of coarse grains in the weld zone and heat-affected zone (HAZ) of fusion welds. This results in deterioration of both toughness and ductility (Ref 2). On the other hand, susceptibility to intergranular corrosion (IGC) caused by the depletion of chromium content in the vicinity of HAZ is a major concern affecting the full deployment of this material in certain engineering application, regardless of its attractive economics combined with moderate strength and excellent corrosion resistance in caustic and acidic environments. This susceptibility is broadly termed as sensitization (Ref 3). In our previous study, the application of modified Strauss test to evaluate the sensitization resistance of AISI 409M FSS welds by weight loss measurements were reported (Ref 4).

The degree of sensitization (DOS) can be determined by weight loss measurements, but these techniques are complicated by the deposition of copper on the sample, necessitating complete removal before accurate weight measurement and

also this method is time consuming. Quantitative results can therefore more readily be obtained most accurately by electrochemical methods. Electrochemical evaluation techniques for IGC have generally found acceptance for austenitic and high chromium FSS (Ref 5), but their application to low chromium steels has been limited. This is largely due to the concern that these methods will not be effective on a dual-phase microstructure and that preferential attack on martensite will overshadow the response attributable to IGC (Ref 6). However, the effect of second phase such as martensite can be identified from the additional reactivation loops in electrochemical potentiokinetic reactivation (EPR) curve as reported by Cihal (Ref 7). In addition to quick and reliable detection of sensitization in 12% Cr FSS, EPR test also indicates the corrosion stability of martensite phase present in the microstructure of these alloys. Tomlinson and Mathews (Ref 8) in their study on sensitization behavior of gas tungsten arc welded AISI 405 stainless steel reported that, the HAZ suffered from intergranular attack, which can be eliminated by proper annealing treatment.

AISI 409M is a low-chromium FSS that performs well in many wet sliding abrasion applications and in aqueous environments, often replacing coated carbon and galvanized steels in mildly corrosive surroundings (Ref 9). Using AISI 409M grade FSS for structural application in corrosive environments will be economical, as it imparts acceptable corrosion resistance using minimum Cr content. However, sensitization of stainless steel during thermo-mechanical processing and welding has been a major challenge to face.

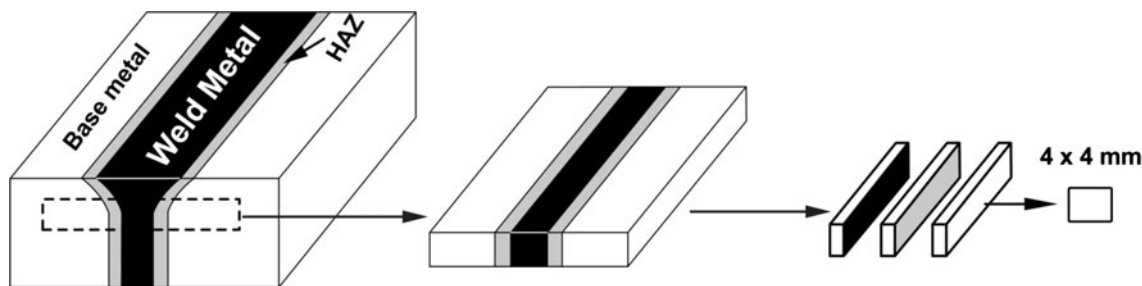
In a recent study by Sahoo et al. (Ref 10), it was reported that the HAZ of shielded metal arc welded AISI 409M FSS joints exhibited similar sensitization resistance as of the base metal (BM). However, the welding conditions and relevant microstructures prior and after DL-EPR test at higher magnification were not disclosed by the authors. Low chromium (with 11.4%) AISI 409M grade stainless steels are susceptible to IGC, when improper welding conditions are used. The susceptibility of these alloys is strongly influenced by microstructural changes due to different welding processes applied to obtain good mechanical properties.

By keeping all the above facts in mind, this investigation was carried out to assess the sensitization resistance of AISI 409M FSS joints fabricated by four different welding processes

A.K. Lakshminarayanan, Department of Mechanical Engineering, SSN college of Engineering, Kalavakkam, Chennai 603 110 Tamil Nadu, India; and V. Balasubramanian, Department of Manufacturing Engineering, Centre for Materials Joining & Research (CEMAJOR), Annamalai University, Annamalai Nagar, Chidambaram 608 002 Tamil Nadu, India. Contact e-mails: akln2k2@yahoo.com, lakshminarayananak@ssn.edu.in, and balasubramanian.v.2784@annamalaiuniversity.ac.in.

Table 1 Chemical composition (wt.%) of BM (measured through spectrometry)

Material	C	Mn	P	S	Si	Cr	Ni	Ti	Fe
Base Metal (AISI 409M)	0.028	1.10	0.030	0.010	0.40	11.40	0.39	0.004	Bal.

**Fig. 1** Scheme of extraction of specimens for sensitization (DL-EPR) test

namely friction stir welding (FSW), laser beam welding (LBW), electron beam welding (EBW), and gas tungsten arc welding (GTAW) through double loop electrochemical potentiokinetic reactivation (DL-EPR) tests.

2. Experimental Procedure

2.1 Base Metal

The as-received base metal used in this study was 4 mm thick cold rolled, annealed, and pickled AISI 409M grade FSS plates. The chemical composition of the BM measured using vacuum spectrometer is presented in Table 1.

2.2 Weld Joints

Few welding trials were carried out using GTAW, LBW, EBW, and FSW processes without filler metal additions. Specimens were extracted from various locations of the joint and subjected to macrostructural analysis. The specimen free of volumetric defect and with complete penetration was considered as the optimized welding condition. The welding conditions and optimized process parameters can be obtained from elsewhere (Ref 4).

2.3 Specimen Preparation

Specimens of 4×4 mm (as shown in Fig. 1) were prepared using metallurgical sample saw (Make: Ducom, India; Model: MS-10) from both the weld metal, and HAZ of welded joints as per ASTM G108-07 guidelines. The specimens prepared from the welded joints were polished using standard metallographic procedures to obtain flat and scratch-free surface. Polishing were done mechanically before DL-EPR using different grades of emery papers and a final diamond paste polish to yield a $1 \mu\text{m}$ surface finish. The exposure of 4 mm square area to the electrolyte was ensured. The rest of the area was covered with an acid resistant lacquer after polishing. The photographs of prepared specimens for DL-EPR analysis are displayed in Fig. 2.

**Fig. 2** EPR test samples

2.4 Double Loop Electro Potentiokinetic Reactivation Test

DL-EPR testing was performed as per ASTM G108-07 standard with a Gill AC Potentiostat in conjunction with an ASTM standard cell, personal computer, and software for data collection. A 2.5 cm^2 platinum flag counter electrode and a saturated calomel reference electrode (SCE) were used. The samples were polarized at a scan rate of 12 V/h starting from the corrosion potential, which is approximately -600 mV (SCE) for this material. The tests were conducted at $28 \pm 1 \text{ }^\circ\text{C}$ in deoxygenated $\text{H}_2\text{SO}_4 \cdot 0.1 \text{ M} + \text{Na}_2\text{SO}_4 \cdot 0.4 \text{ M} + \text{KSCN} 1000 \text{ ppm}$ and pH value of 1.6. Each test was carried out thrice in order to assure its repeatability. After DL-EPR analysis, the morphologies of IGC attack were observed by scanning electron microscopy. The extent of sensitization is determined by the ratio of the reactivation current (I_r) and the activation current (I_a), where a low I_r/I_a ratio indicates a lower DOS.

2.5 Microstructural Analysis

Microstructure of the as-welded specimens prior to DL-EPR testing was examined using transmission electron microscopy

(TEM). Thin foils with a thickness of about 1 mm were cross-sectioned from the welded joints to prepare the TEM samples. After being mechanically ground to approximately 80 μm , the foils were further ground to a thickness of 15 μm by a dimple grinding machine. Then the electron transparent thin sections were electrolytically prepared by the twin-jet polisher. An

electrolyte of 10% perchloric acid + 90% ethanol solution ($-25\text{ }^\circ\text{C}$) was used during thinning. These thin foils were observed under a 200 kV potential using a transmission electron microscope (Make: Philips, UK: Model: CM20). Microstructure of the specimens after DL-EPR test was analyzed using scanning electron microscopy. Energy dispersive x-ray spectrometry (EDAX) line scan was used to determine the distribution of chromium across the grain boundaries of HAZ of all the four joints

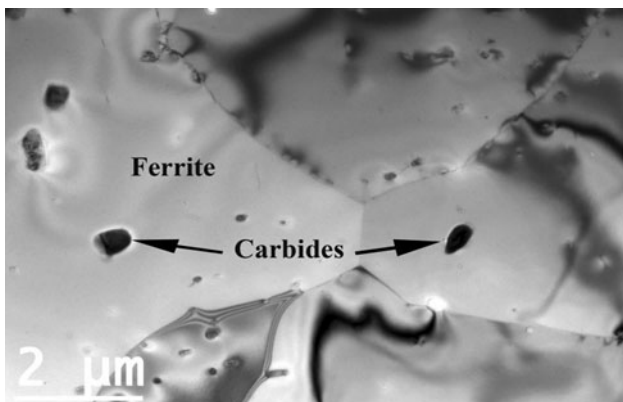
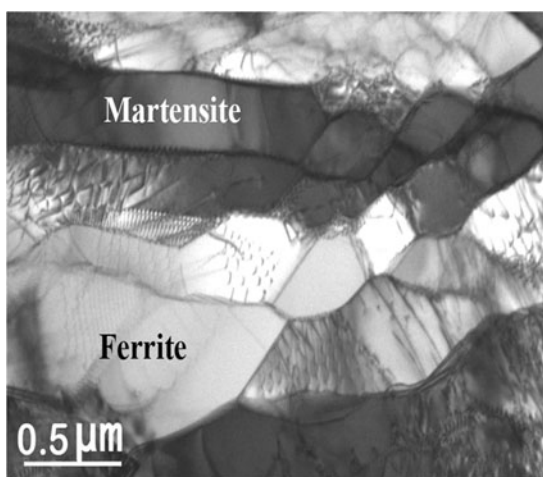


Fig. 3 Transmission electron micrograph of the BM

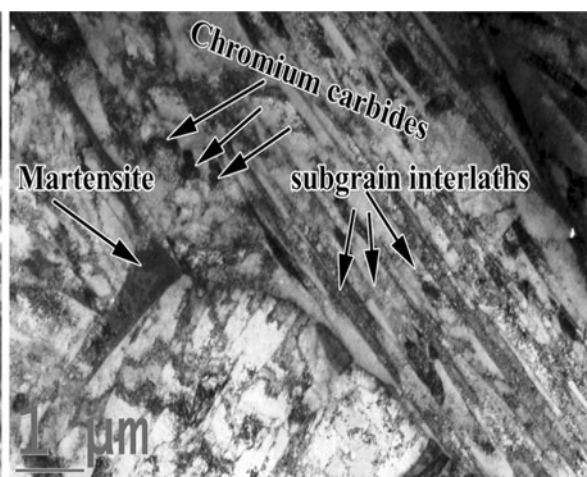
3. Results and Discussion

3.1 Microstructure Analysis Prior to EPR Testing

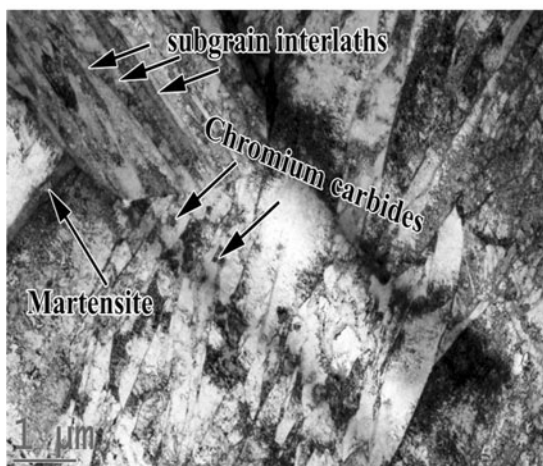
TEM image (Fig. 3) of BM shows the characteristics of grain boundaries with ferrite grains and the presence of Cr_{23}C_6 carbides. TEM image of stir zone (Fig. 4a), comprises the banded microstructure of ferrite and martensite. Stir zone (SZ) showed a mixed deformation structure with equiaxed ultrafine grains and the cellular substructure between martensite laths. Severe deformation due to friction stirring resulted in the formation of fine subgrained structure, which propagates



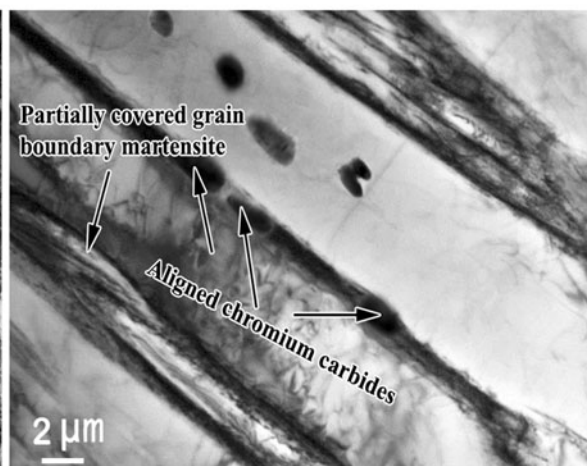
(a) FSW-SZ



(b) EBW-FZ



(c) LBW-FZ



(d) GTAW-FZ

Fig. 4 Transmission electron micrographs of weld metal region

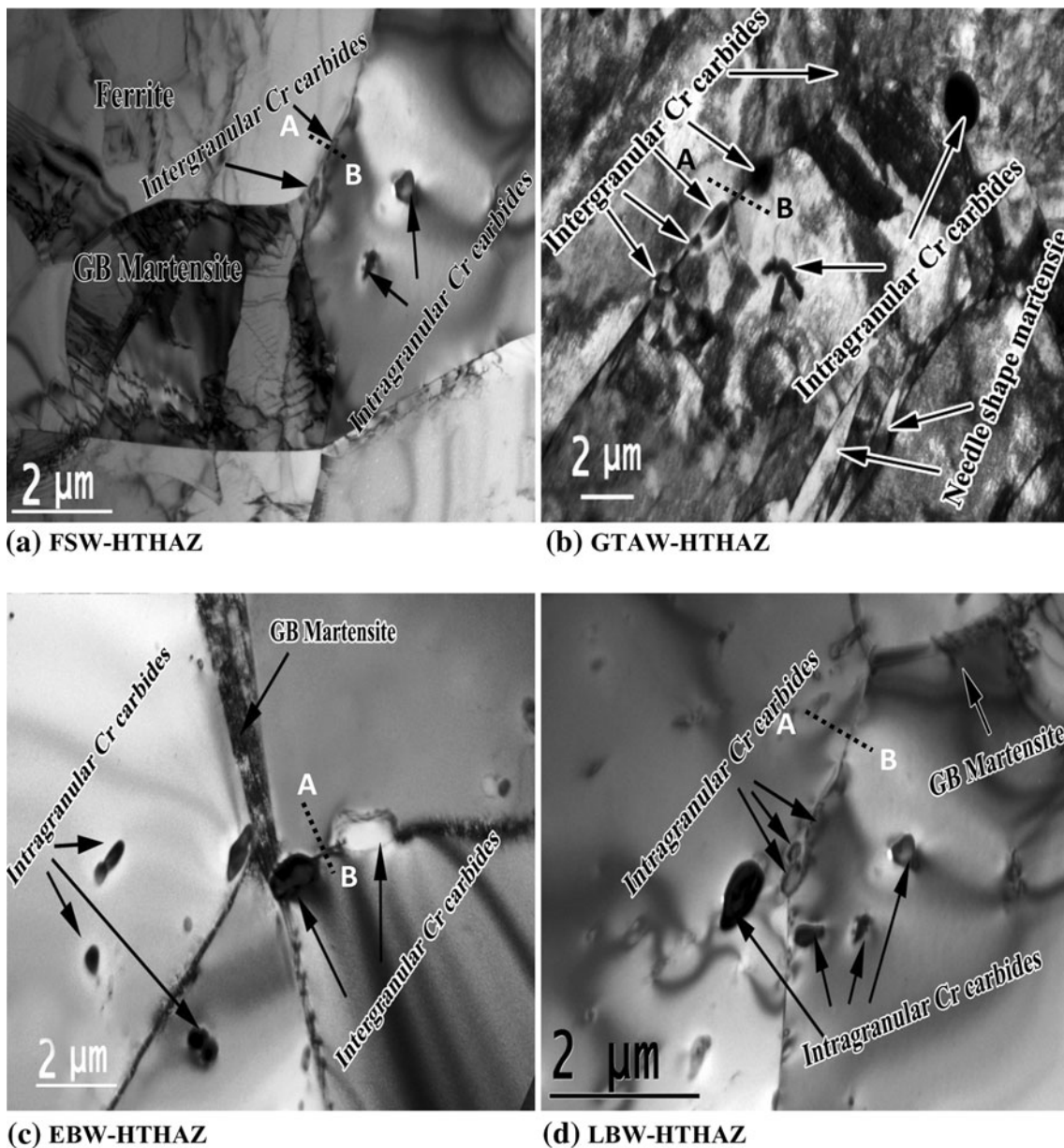


Fig. 5 Transmission electron micrographs of HTHAZ

throughout the ferrite grains. This strain-induced submicrocrystalline structure involves highly misoriented equiaxed grains with a relatively low dislocation density in their interiors as compared with high dislocation densities in cell substructures, which evolve at smaller strains. The presence of high dislocation density in the substructure discloses that the SZ had undergone strain hardening during welding.

TEM image of fusion zone (FZ) of EBW joint (Fig. 4b) clearly shows the presence of prior δ ferrite grain boundaries, substructure, and subgrain structure. The presence of chromium carbides and grain boundary martensite are also evidenced from Fig. 4b. This suggests that the equiaxed coarse grain structure in BM undergone a refinement during weld thermal cycle. Similar microstructure was observed in the FZ of LBW joint. The difference in FZ microstructure between EBW joint and LBW joint is the degree of fineness in the subgrain structure. In LBW joint (Fig. 4c), the ferrite lath

width is comparatively smaller than the width of the ferrite lath evolved in EBW joint. Coarse lath ferrite structure with partially covered needle-shape martensite and chromium carbides decorated grain boundaries was observed in case of GTAW joint (Fig. 4d).

High temperature heat-affected zone (HTHAZ) of all the four joints was analyzed using TEM and the resultant images are presented in Fig. 5. The HTHAZ of FSW joint (Fig. 5a) also shows a duplex structure of ferrite and martensite. The martensite is formed along many subgrain boundaries of the ferrite as well as in the grain boundaries. Chromium carbides are also observed in some of the grain boundaries. Dislocations are observed both in ferrite and martensite of this region. It indicates that this region undergone partial plastic deformation during FSW. The HTHAZ of GTAW joint (Fig. 5b) shows a mixed microstructure of ferritic grains with both intra and intergranular chromium carbides. The growth of ferrite was

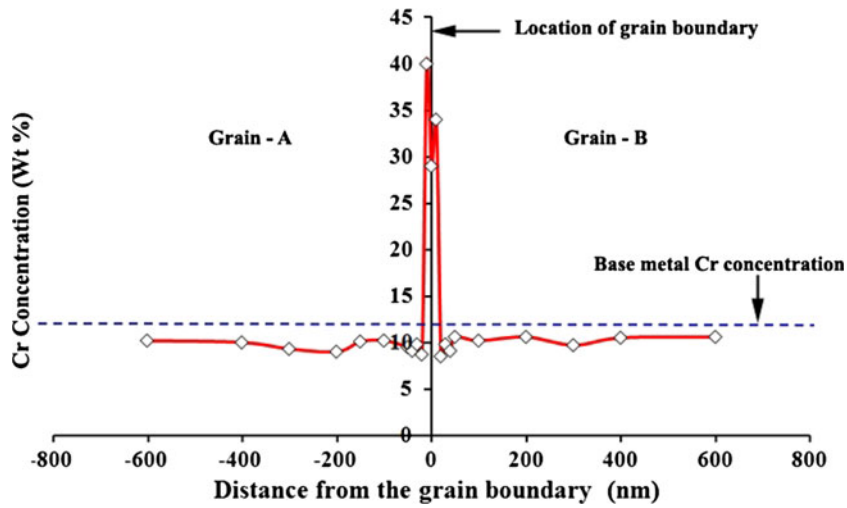


Fig. 6 Cr concentration profile across grain boundary in GTAW joint

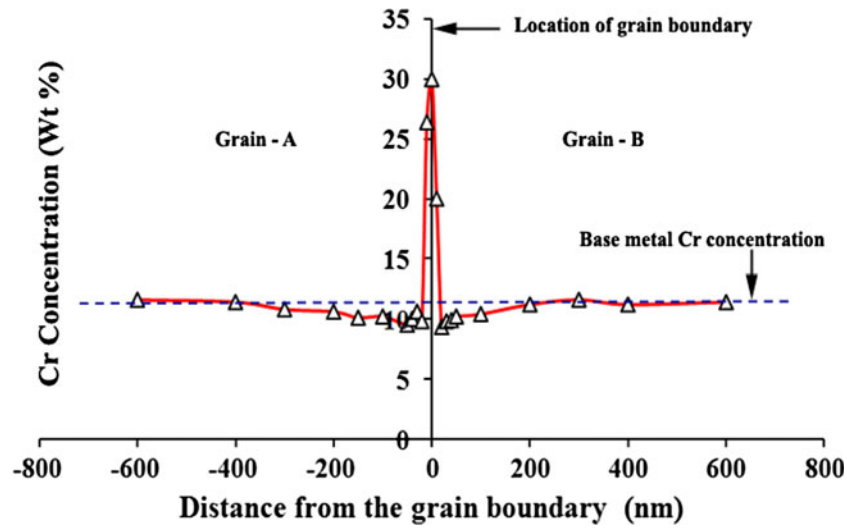


Fig. 7 Cr concentration profile across grain boundary in LBW joint

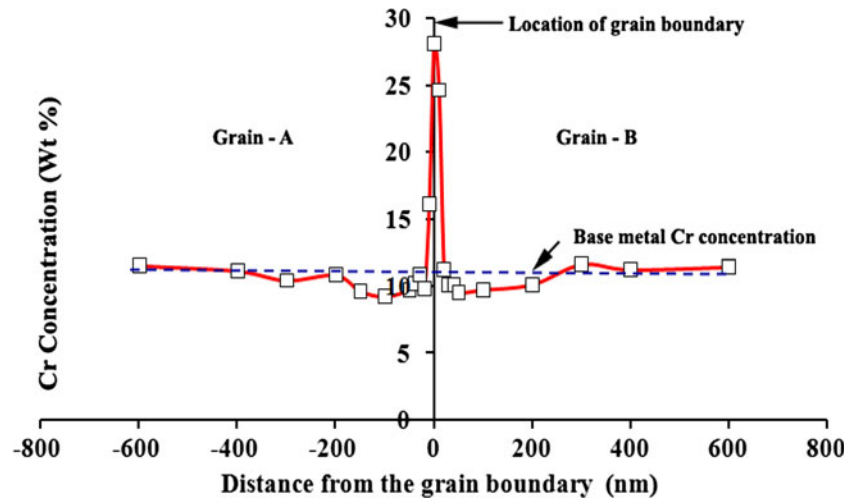


Fig. 8 Cr concentration profile across grain boundary in EBW joint

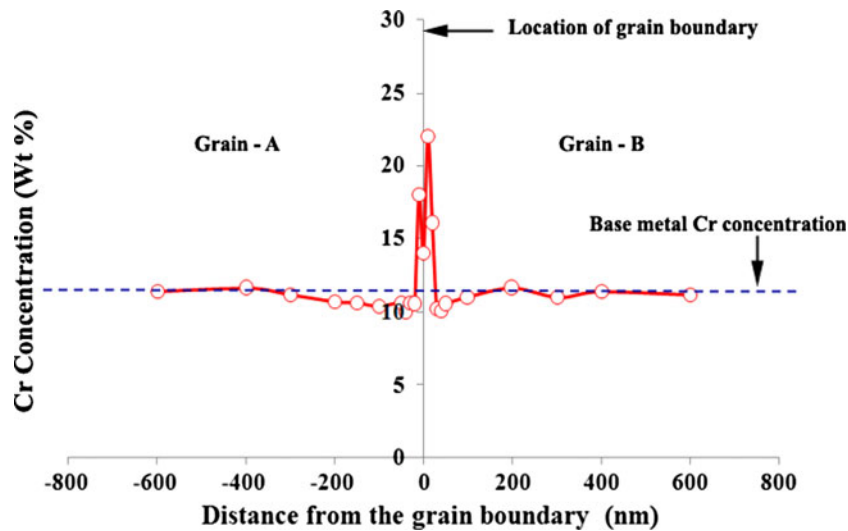


Fig. 9 Cr concentration profile across grain boundary in FSW joint

accompanied by the precipitation of carbides at moving interface and this result in the aligned precipitation, which follows the shape of ferrite grain. Coarse plate-like martensite and needle-shape martensite along with the grain boundaries of ferrite are also observed in the HTHAZ. The HTHAZ of LBW and EBW joints (Fig. 5c, d) shows mostly of ferritic structures enriched with grain boundary chromium carbides. Low carbon lath martensite is also observed at the grain boundaries.

3.2 Cr profile Across the Grain Boundaries

From TEM analysis, it can be observed that, the grain boundaries of HAZ of the welded joints are enriched with Cr_{23}C_6 chromium carbides. It is likely that the Cr-depleted zone is formed in the vicinity of the grain boundaries. Therefore, the Cr profiles across the grain boundaries having the Cr-rich carbides were measured in the HAZ of the welded joints by TEM/EDAX and they are displayed in Fig. 6, 7, 8, and 9. The Cr profiles were obtained along the dotted lines in the TEM images presented in Fig. 5. The grain boundaries of the HAZ have remarkably higher Cr content than those inside the grains. Of the four joints, GTAW joint showed higher Cr content in the grain boundaries and wider Cr-depleted region compared to other joints. Minimum Cr contents in the Cr-depleted zones were approximately 9.2, 10.1, 9.6, and 9.8 wt.% in the GTAW, FSW, LBW, and EBW, respectively, i.e., the HAZ of GTAW joint has slightly deeper Cr depletion than the other joints.

3.3 Degree of Sensitization

Figure 10(a) shows a schematic plot of the definitive EPR conditions used. Sensitization evaluation is assessed through the maximum currents of each loop. The peak anodic current is referred to as I_a and the peak reactivation current is defined as I_r . The DOS is defined by the ratio of I_r/I_a .

Figure 10(b) shows a typical DL-EPR curve for AISI 409M FSS base metal. During the forward scan, the BM gives a single corrosion potential as is usual with a single peak located at the passivation potential of -25 mV (SCE), respectively, with an activation current density of 45.6 mA/cm². In the reactivation scan, BM curve shows a single reactivation peak centered at approximately -350 mV (SCE), which can be associated with

an attack at Cr-impoverished grain boundaries. However, since the BM is in annealed and desensitized condition, the reactivation current density is much lower than the activation current density and hence it showed lower DOS. The EPR curves of fusion zone (FZ) and HTHAZ of all the four joints were obtained from DL-EPR test and they are presented individually for clarity in Fig. 10 and 11, respectively. The EPR curves presented in Fig. 10 and 11 were analyzed for various features such as peak broadening due to martensitic dissolution during reactivation, anodic and reactivation current density, etc., and results are presented in Table 2.

Figures 10(c) and 11(a) show the EPR curves of the HTHAZ and SZ of the FSW joint, respectively. Generally, in cases where other kinds of attack superimpose on IGC, additional reactivation loops may be present in EPR curve. As pointed out by other authors (Ref 11, 12), each loop, identified by its own peak potential, may generally be correlated to the attack at a well-defined phase or zone of a material. Based on these considerations, the EPR test is expected to discriminate between the general dissolution of martensite and reactivation of chromium-depleted areas, provided that, they manifest themselves in separate and distinct regions of the EPR curve. Such behavior is clearly observed in EPR curves obtained from of weld metal region of the joints.

The shape of reactivation curve obtained for stir zone is quite different from HAZ region. The anodic reactivation peak current density increased constantly, until the peak current densities (I_r) were reached. The I_r values depend closely on dissolution reaction of the phases in the metal, since during the reactivation sweep only the sensitized areas contribute to passive-active transition.

The reactivation curve of stir zone consists of two separate and distinct regions. The first peak visible as a broad anodic shoulder in the range 0 to -300 mV (SCE) can reasonably be associated with preferential dissolution of martensitic phase present in stir zone, which is occurring before the reactivation potential on the grain boundaries is reached. In addition, a general reactivation, possibly associated with attack of chromium-depleted zones along grain boundaries separating the ferrite and martensite phases, is also revealed with second peak located at -400 mV (SCE). These observations, splitting of the

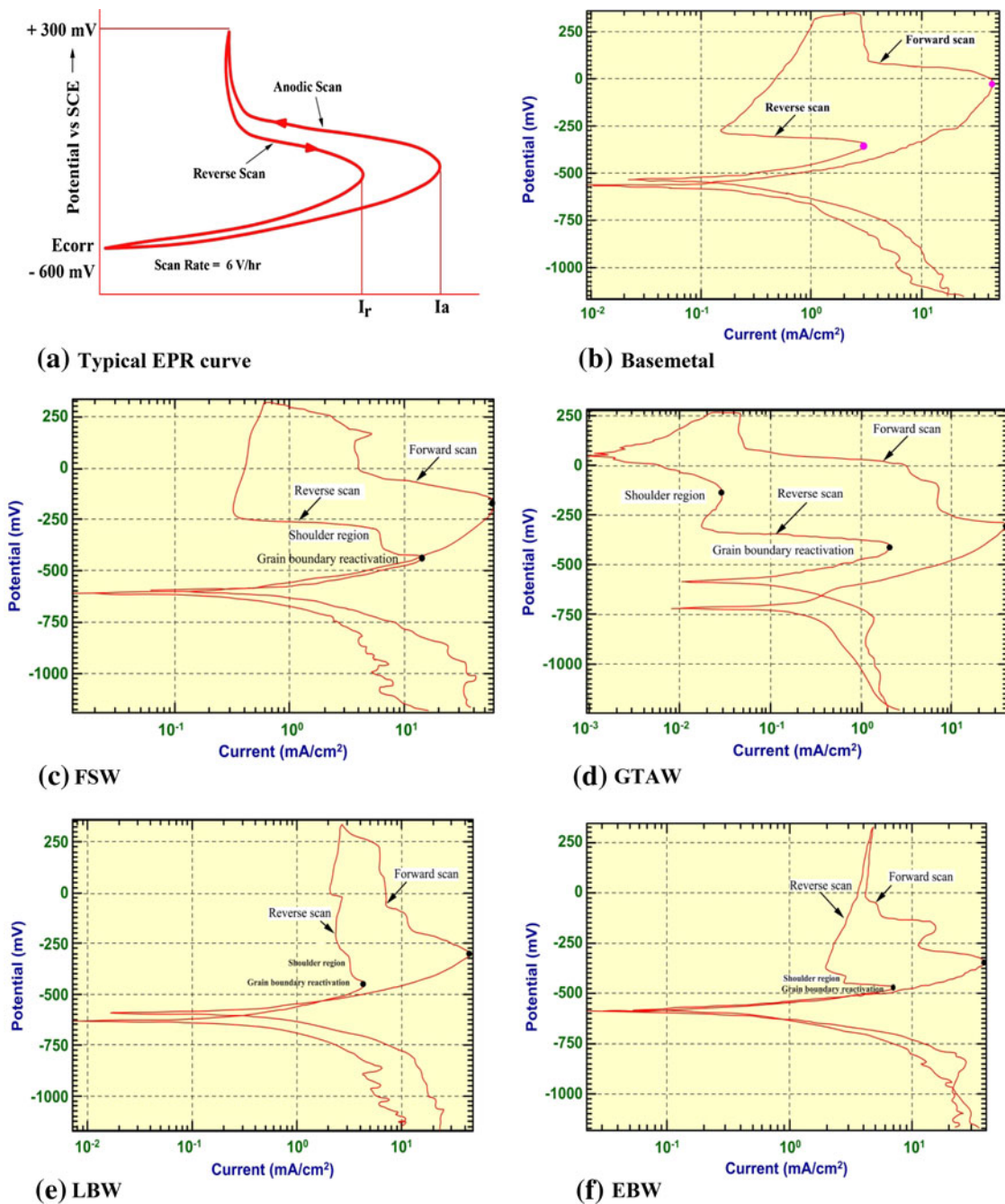


Fig. 10 DL-EPR curves for weld metal region of AISI 409M FSS joints

peak of reactivation curve in the samples having both martensitic and ferritic phases, are in agreement with the findings of Cihal (Ref 7). However, the reactivation current density is nearly same as of the BM and hence SZ of FSW joint exhibited lower DOS compared to other joints. On the other hand, HTHAZ of FSW joint shows single reactivation peak and slightly higher DOS.

From Fig. 10(d) and 11(b), it can be inferred that the FZ and HTHAZ of GTAW joint shows very poor sensitization resistance. EPR curves of FZ also displays dual peak during the reactivation scan. However, this is not as much wider as seen in FSW joint and this implies that majority of dissolution is mainly being associated with the severe attack at Cr-impoverished grain boundaries. EPR curve of HTHAZ region shows

single peak during both forward and reverse scan. However, FZ and HTHAZ of GTAW show higher DOS when compared to other joints.

From Fig. 10(e), (f), and 11(c), (d), it can be seen that the FZ and HTHAZ of LBW and EBW joints were also sensitized. FZ of both the joints shows much smaller shoulder region associated with martensite dissolution. The FZ also exhibited minimum DOS when compared to HTHAZ. Also, HTHAZ of LBW joint exhibited higher DOS when compared to EBW and FSW joints. The results obtained from DL-EPR analysis is summarized in Table 2.

DOS of WM region and HTHAZ are compared in the form of bar graphs as shown in Fig. 12. It can be inferred that, HTHAZ and SZ exhibited lower DOS compared to all other

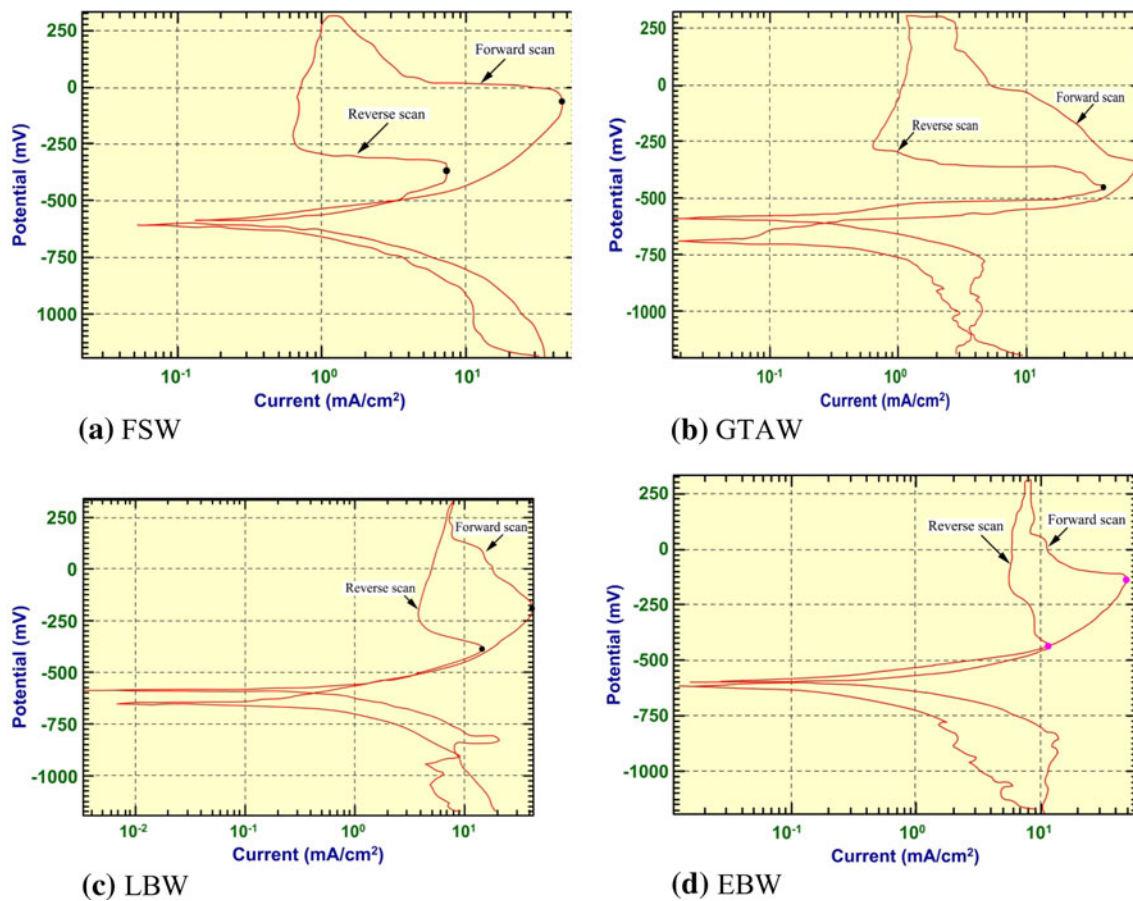


Fig. 11 DL-EPR curves for HTHAZ of AISI 409M FSS joints

Table 2 EPR Test data sheet

Specimen	I_a	I_r	Forward peak potential, mv	Reverse peak potential, mv			DOS, %
				Shoulder	Grain reactivation	Corrosion potential	
BM	45	2.9	-50	...	-350	-550	4.30
FSW-SZ	40	2.5	-200	-175	-375	-700	6.20
FSW-HAZ	38	7.5	-150	...	-350	-575	14.4
GTAW-FZ	60	15	-200	-300	-425	-650	25.0
GTAW-HAZ	80	42	-350	...	-450	-725	52.5
EBW-FZ	40	7	-300	-425	-500	-600	10.0
EBW-HAZ	50	11.25	-150	...	-400	-625	22.5
LBW-FZ	40	4.5	-300	-400	-450	-650	11.3
LBW-HAZ	42	15.75	-160	...	-375	-625	37.5

joints. This indicates that, grain boundaries in SZ are not sensitized or with minimal sensitized boundaries. However, the overall corrosion rate is higher for FSW joint compared to LBW and EBW joints. This is mainly due to corrosion attack on martensite phase and also the larger width of WM region.

3.4 Microstructure Analysis After EPR Test

Microstructural analysis was carried out on DL-EPR test specimens and displayed in Fig. 13. Figure 13(a) shows the SZ microstructure of FSW joint and it shows a dual-phase microstructure with isolated ditches at the ferrite-ferrite grain boundaries. In some regions of SZ, the martensite dissolution was also occurred. Figure 13(b) shows the lath ferrite with some grain

boundary martensite, ditches at the grain boundaries, and a generalized attack inside the grains. The ditches indicate that chromium-rich phases were precipitated at the grain boundaries and the generalized attack indicates that the chromium carbides also precipitated inside the grains.

Figure 13(c) and (d) shows the FZ microstructure of LBW and EBW joints, respectively, after DL-EPR test. Ditched grain boundaries and pits are visible at few regions. Figure 14 displays the SEM image of HTHAZ of the welded joints after EPR test. Intergranular attack is observed in all the cases. Grain dropping caused from IGC was also observed in the HTHAZ of the welded joints. However, severity of the attack is very high in case of GTAW joint compared to the other joints.

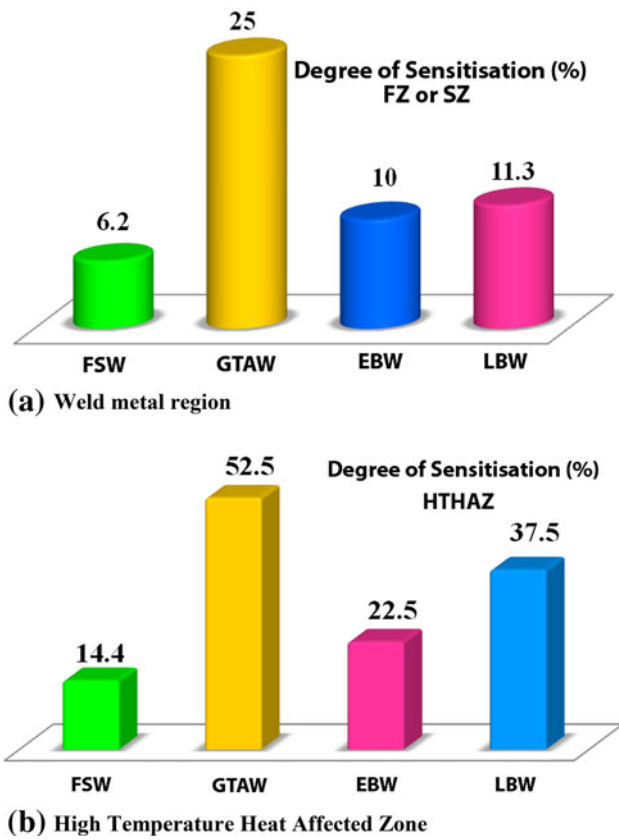


Fig. 12 Effect of welding processes on the DOS

4. Discussion

Double loop electrochemical potentiokinetic reactivation test was used to assess the sensitization resistance of AISI 409M FSS weldments. Of the four joints produced, the FSW joints showed the least DOS when compared to LBW, EBW, and GTAW joints. The difference in sensitization resistance of welded joints largely depends on the microstructural changes that occur due to the individual welding process characteristics.

LBW and EBW are high energy density processes which involves rapid heating and cooling thermal cycles resulting into lower specific heat input to the weld metal region (Ref 13). Although GTAW process is also a fusion welding process like LBW and EBW processes, there is notable difference in the thermal cycles and heat input which influences the weld microstructure and subsequently its corrosion properties (Ref 14). On the other hand, FSW is solid state process and hence, the heat input is lower compared to GTAW process.

Greef et al. (Ref 15) investigated the effect of heat input on sensitization resistance of gas tungsten arc welded low chromium FSS and it was found that the joints produced with both lower and higher heat input showed severely sensitized grain boundaries. From the DL-EPR test conducted in this study, it was observed that the current ratio (i.e., DOS) recorded in weld metal and HAZ of GTAW joint was higher followed by LBW and EBW joints. FSW joints exhibited lower DOS compared to other joints due to the optimum heat input and solid state nature of process.

Predicting the sensitization behavior of AISI 409M during weld thermal cycles is complicated by the presence of the

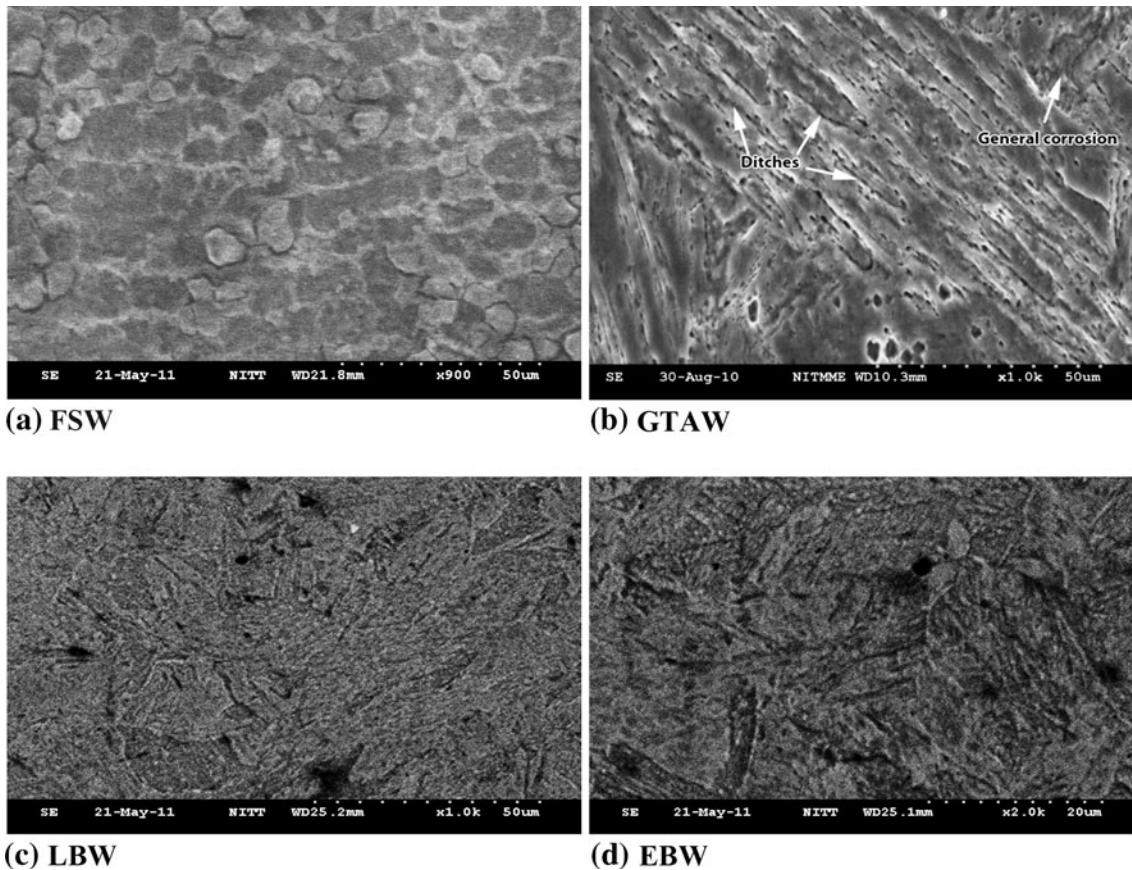


Fig. 13 SEM image of weld metal region after DL-EPR test

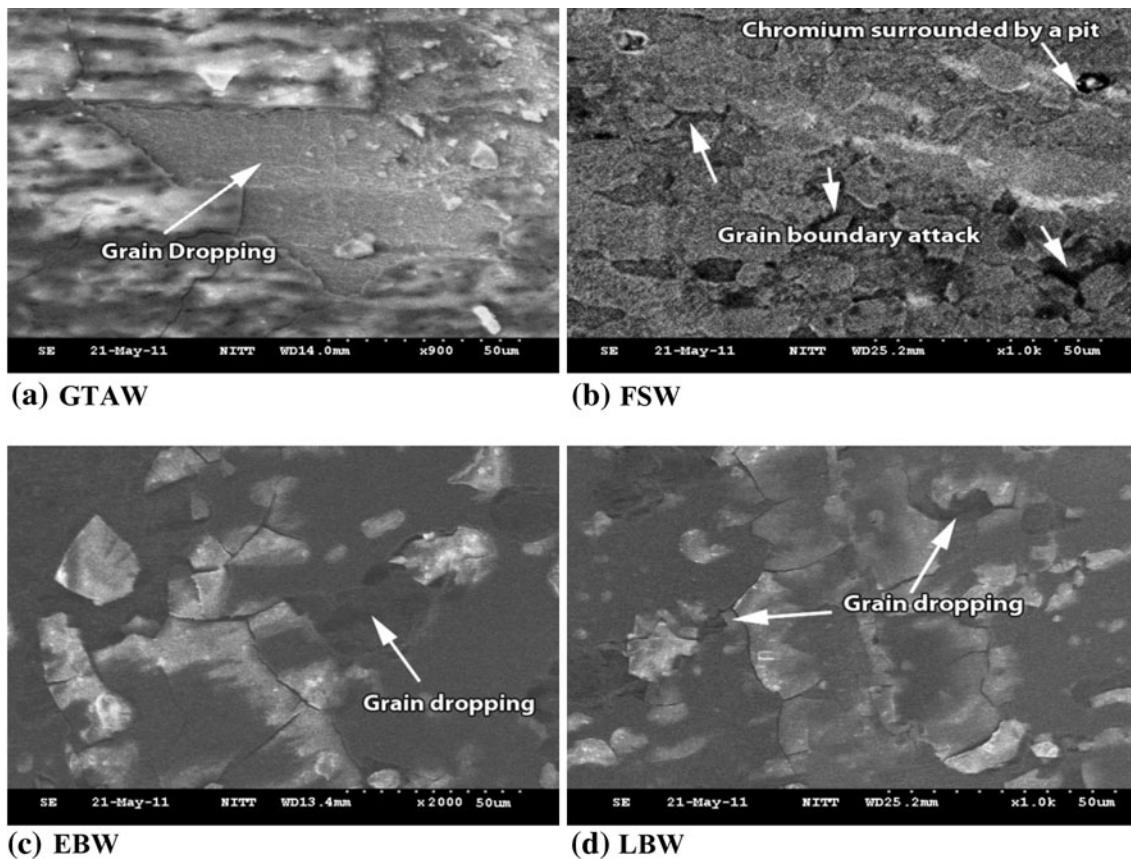


Fig. 14 SEM image of HTHAZ after DL-EPR test

so-called gamma loop in the typical Fe-Cr phase diagram presented elsewhere (Ref 16). In LBW and EBW, rapid cooling rates suppressed austenitic nucleation as the HTHAZ cools down through the dual-phase region and resulted in fully ferritic HTHAZ microstructure. Excessive carbide precipitation occurred in the ferrite-ferrite grain boundaries due to lower solubility of carbon in ferrite phase and this resulted in chromium depletion at the grain boundaries of LBW and EBW joints. This is evidenced in and well detected by EPR curve (Fig. 11c, d). Fusion zone of LBW and EBW joints showed lower DOS compared to HTHAZ and it is mainly due to relatively higher peak temperature which resulted in formation of sufficient martensite phase and this avoided the continuous network of chromium-depleted zone that minimized the sensitization. This can be inferred from Fig. 5 and 10(e), (f).

Higher heat input levels supplied during GTAW joints led to longer residence times above the A1 temperature during welding, resulting in grain growth in the FZ and HTHAZ with majority of ferrite-ferrite grain boundaries and ferrite with partially covered martensite and chromium carbides. Also unstabilized low Cr steels used in this study suffers from sensitization of austenite (martensite) under very slow cooling conditions. The difference in sensitization caused by chromium and martensite phase is well distinguished in EPR curves presented in Fig. 10(c).

FSW of modified 12% Cr stainless steel was carried out in a dual-phase region of austenite and ferrite and during cooling cycle, the austenite was transferred to martensite in the stir zone and hence stir zone consists of very fine and roughly equal amount of ferrite and martensite. The presence of martensite

increases the phase boundary area due to inherently finer grain size. Finer grain size in the stir zone is also one of the reasons for improved sensitization resistance compared to other joints. This is mainly because of the profusion of grain interiors to the grain boundary Cr-depleted regions and so desensitization almost occurs simultaneously with sensitization as reported by Beltran et al. (Ref 17) and Dischino et al. (Ref 18). HAZ of FSW joint showed higher DOS when compared to the SZ and this is mainly due to the peak temperature difference and amount of martensite present in the HAZ region. The peak of the reverse branch of EPR curve due to reactivation of ferritic-ferrite Cr-depleted grain boundaries was identified from EPR curve of BM and compared with weld metal region. DL-EPR test clearly discriminated the martensitic dissolution and reactivation of chromium-depleted zone by separate and distinct regions of the EPR curve (Fig. 10c).

5. Conclusions

The influences of welding processes on sensitization behavior of AISI 409M FSS joints was studied using DL-EPR test and the following important conclusions were derived from this investigation:

- Stir zone of FSW joint exhibited low DOS which is 75.2, 45.13, and 38.0% lower, when compared to the fusion zone of GTAW, LBW, and EBW joints, respectively. This is mainly due to formation of fine grains which reduces the time required for desensitization.

- The HTHAZ of all the four joints suffered from sensitization. Of the four joints, the joint fabricated using GTAW process showed higher DOS and least sensitization resistance, which is 264, 133, and 40% higher, when compared to FSW, EBW, and LBW joints, respectively. This is mainly due to the ferrite grain growth with grain boundary chromium carbides caused by higher heat input supplied by the process.
- The corrosive attack on martensite phase and by chromium carbide precipitation of modified 12% Cr FSS welds was clearly distinguished by separate and distinct regions of the reactivation curve of DL-EPR test.

Acknowledgments

The authors wish to place their sincere thanks to the Department of Science and Technology (DST), Government of India for the financial support through Fast Track Scheme for Young Scientists R&D project (SR/FTP/ETA043/2009) to carry out this investigation.

References

1. J.C. Lippold and D. J. Kotecki, *Welding Metallurgy and Weldability of Stainless Steels*, Wiley, New York, 2005, p 87–88
2. E. Deleu, A. Dhooge, E. Taban, and E. Kaluc, Possibilities and Limitations to Improve the Weldability of Low Carbon 12Cr Ferritic Stainless Steel for Expanded Industrial Applications, *Weld. World*, 2009, **53**, p R198–R208
3. M.O.H. Amuda and S. Mridha, An Overview of Sensitization Dynamics in Ferritic Stainless Steel Welds, *Int. J. Corr.*, 2011, **2011**, 305793. doi:10.1155/2011/305793
4. A.K. Lakshminarayanan and V. Balasubramanian, Assessment of Sensitization Resistance of AISI, 409M Grade Ferritic Stainless Steel Joints Using Modified Strauss Test, *Mater. Des.*, 2012, **39**, p 175–185
5. R.A. Lula and J.A. Davis, Intergranular Corrosion in 12 Percent Chromium Ferritic Stainless Steels, *Intergranular Corrosion of Stainless Alloys. ASTM STP 656*, R.F. Steigerwald, Ed., ASTM, 1978, p 233–247
6. M. Van Warmelo, D. Nolan, and J. Norrish, Mitigation of sensitisation Effects in Unstabilised 12% Cr Ferritic Stainless Steel Welds, *Mater. Sci. Eng. A*, 2007, **464**, p 157–169
7. V. Cihal, A Potentiokinetic Reactivation Method for Predicting the I.C.C. and I.G.S.C.C. Sensitivity of Stainless Steels and Alloys, *Corr. Sci.*, 1980, **20**, p 737–745
8. W.J. Tomlinson and S.J. Matthews, Intergranular Corrosion of Welds in Type 405 Stainless Steel, *J. Mater. Sci.*, 1988, **23**, p 2064–2068
9. M. Mukherjee and T.K. Pal, Influence of Heat Input on Martensite Formation and Impact Property of Ferritic-Austenitic Dissimilar Weld Metals, *J. Mater. Sci. Technol.*, 2012, **28**, p 343–352
10. G. Sahoo, K. Ravi, and S. Srikanth, Corrosion of 12% Ferritic Steel and Weld Joints in H₂SO₄ Environments, *Steel Grips*, 2008, **6**, p 441–444
11. S. Frangini and A. Mignone, Modified Electrochemical Potentiokinetic Reactivation Method for Detecting Sensitization in 12 wt.% Cr Ferritic Stainless Steels, *Corrosion*, 1992, **48**, p 716–726
12. B. Poulson, The Sensitization of Ferritic Steels Containing Less Than 12% Cr, *Corr. Sci.*, 1978, **18**, p 371–395
13. H.T. Lee and J.L. Wu, The Effects of Peak Temperature and Cooling Rate on the Susceptibility to Intergranular Corrosion of Alloy 690 by Laser Beam and Gas Tungsten arc Welding, *Corr. Sci.*, 2009, **51**, p 439–445
14. H. Zheng, X. Ye, L. Jiang, B. Wang, Z. Liu, and G. Wang, Study on Microstructure of Low Carbon 12% Chromium Stainless Steel in High Temperature Heat-Affected Zone, *Mater. Des.*, 2010, **31**, p 4836–4841
15. M.L. Greef and M. Du Toit, Looking at the Sensitization of 11–12% Chromium EN 1.4003 Stainless Steels During Welding, *Weld. J.*, 2006, 243-s–251-s
16. A.K. Lakshminarayanan and V. Balasubramanian, Characteristics of Laser Beam and Friction Stir Welded AISI, 409M Ferritic Stainless Steel Joints, *J. Mater. Eng. Perform.*, 2012, **21**, p 530–539
17. A. Dischino and J.M. Kenny, Effect of Grain Size on the Corrosion Resistance of a High Nitrogen-Low Nickel Austenitic Stainless Steel, *J. Mater. Sci. Lett.*, 2002, **21**, p 1969–1971
18. R. Beltran, J.G. Maldonado, and L.E. Murr, Effects of Strain and Grain Size on Carbide Precipitation and Corrosion Sensitization Behavior in 304 Stainless Steel, *Act. Mater.*, 1997, **45**, p 4351–4160